Hindawi
Shock and Vibration
Volume 2024, Article ID 1843652, 13 pages
https://doi.org/10.1155/2024/1843652

Research Article

Research on the Load Bearing and Impact Resistance of a Novel Structure Exhibiting Both Positive and Negative Poisson's Ratios

Xidong Zhang, Hongyu Cui, Haoming Hu, Xiaokai Yin, and Huanqiu Xu

State Key Laboratory of Structural Analysis for Industrial Equipment, School of Naval Architecture and Ocean Engineering, Dalian University of Technology, Dalian 116024, China

Correspondence should be addressed to Hongyu Cui; cuihongyu@dlut.edu.cn

Received 16 November 2023; Revised 7 January 2024; Accepted 20 January 2024; Published 12 March 2024

Academic Editor: Denise-Penelope Kontoni

A ship equipment pedestal is a structure that connects power equipment to a hull. It must have a high load-bearing capacity and the ability to withstand large impact loads. In this paper, a novel structure with a positive-negative Poisson's ratio is proposed. The deformation mechanism and mode of this structure under quasistatic compression loading are analysed via numerical simulation. Based on this new structure, a multicellular pedestal is designed, and its bearing capacity and impact resistance are analysed. The structural parameters of the pedestal are optimized. An experiment is conducted to evaluate the impact resistance of the pedestal model, which confirms that the proposed multicellular pedestal exhibits excellent impact resistance.

1. Introduction

When a ship is subjected to external loads, it can experience instantaneous acceleration that reaches hundreds or even thousands of g due to inertia. Excessive impact loads can cause equipment damage or even failure [1]. The causes of shocks [2, 3] are complex and varied, and there are many kinds of impact protection structures [4–6], most of which are positive Poisson's ratio structures.

A negative Poisson's ratio structure expands under tension and contracts under compression, and its unique behaviour endows it with excellent impact energy absorption performance and fracture resistance, as well as a higher shear modulus [7]. Consequently, a negative Poisson's ratio structure offers a new approach for designing impact protection in marine equipment. Conventional equipment base is difficult to achieve the unity of lightweight structure, impact resistance, and high load capacity. The novel positive and negative Poisson's ratio structure designed in this paper is characterized by high voidage and low density, which meets the requirements of lightweight structures and offers excellent bearing capacity and impact resistance.

In recent decades, research on negative Poisson's ratio structures has developed rapidly, and many novel negative Poisson's ratio structures have been found [8–12]. The deformation mechanisms of negative Poisson's ratio structures are mainly re-entrant and rotational; the re-entrant mechanism is mainly found in star-shaped [13], arrow-shaped [14, 15], and re-entrant-hexagonal [16, 17] structures, while the rotational mechanism is generally more common in chiral [18] and antichiral [19] structures. In 1982, Gibson and Ashby [20] proposed a two-dimensional (2D) re-entrant-hexagonal honeycomb negative Poisson's ratio structure. Grima et al. [21] studied the negative Poisson's ratio effect of a 2D star honeycomb structure. Wang et al. [22] proposed a novel negative Poisson's ratio structure for a re-entrant star-shaped honeycomb by combining the star and re-entrant-hexagonal negative Poisson's ratio structures. Wang et al. [23] proposed a three-dimensional re-entrant honeycomb negative Poisson's ratio structure and analysed the factors affecting the negative Poisson's ratio effect of the structure. Fu et al. [24] proposed a new design concept of a three-dimensional negative Poisson's ratio structure based on the rotational mechanism of a chiral structure. Alomarah et al. [25] proposed a new design concept for a three-dimensional negative Poisson's ratio structure by combining re-entrant and chiral structures. The negative Poisson's ratio structure has been increasingly

widely used in the shipping, automotive, and aviation fields due to its excellent anti-impact vibration isolation performance. Wang et al. [26] designed a cylinder auxetic structure as a suspension jounce bumper for automobiles based on a two-dimensional double-arrow honeycomb and optimized the suspension jounce bumper by using the GA-SQP algorithm. Imbalzano et al. [27] conducted numerical investigations on the dynamic responses and energy absorption properties of hybrid auxetic composite panels (HACPs) and equivalent honeycomb panels (EPPs) subjected to blast loads. HACPs can dissipate and mitigate the imparted energy more efficiently than conventional honeycomb panels. Song et al. [28] designed a new three-dimensional double-arrow negative Poisson's ratio structure for an automobile crash box, which achieved better energy absorption than a traditional crash box. Liu et al. [29] studied the energy-absorbing performance of re-entrant honeycomb and positive hexagonal honeycomb structures under in-plane impact loading. When the same magnitude of compressive strain occurs, the re-entrant honeycomb structure absorbs more energy than the positive hexagonal honeycomb structure. The abovementioned study demonstrated that the re-entrant negative Poisson's ratio structure is better than the traditional structure in terms of anti-explosion and anti-impact effects, anti-impact vibration isolation, and energy absorption effects and has a wide range of application prospects in the impact protection of shipboard equipment.

Based on the demand of a ship equipment pedestal's carrying capacity and impact resistance, a novel positive and negative Poisson's ratio structure is designed in this paper. A numerical simulation method is used to study the deformation mode of the novel structure under quasistatic compression. The ship equipment pedestal is designed based on the novel structure, the impact resistance is verified according to the German military specification BV043/85, and the structural parameter design of the novel positive and negative Poisson's ratio pedestal is optimized. Finally, the impact resistance of the new pedestal structure is verified by an impact test platform.

2. Performance Analysis of Novel Positive and Negative Poisson's Ratio Structures

2.1. Deformation Mechanism of Novel Positive and Negative Poisson's Ratio Structures. A positive Poisson's ratio structure has a high static load-carrying capacity, while a negative Poisson's ratio structure has excellent impact resistance. Based on the demand of ship equipment pedestal load-carrying capacity and impact resistance, a novel positive and negative Poisson's ratio structure cell unit is designed in this paper, as shown in Figure 1. In the study of straight edge structures, stress concentrations will occur at the joint point when force is applied, which reduces the local connection strength. Therefore, a curved edge structure is considered to improve the stress distribution. The design concept mimics the shape of a diamond (the whole cell is an inverted diamond) and combines it with sine and cosine curves.

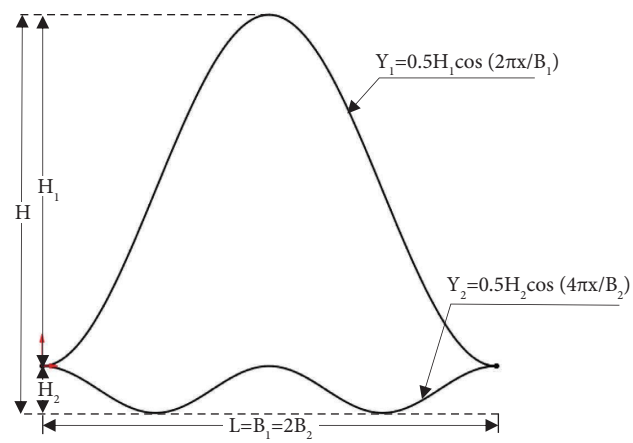

Figure 1: Schematic diagram of the novel cell unit with a positive-negative Poisson's ratio.

The cell unit in Figure 1 comprises two parameterized cosine curves, with the lower curved edge resembling a "W" shape. Hence, this new structure is named the W-shaped arrow (WA) structure. In this structure, the amplitude of the upper and lower cosine curves ($H_1 + H_2$) equals the height of the cell unit (H) and the period length of the cell unit (B_1) corresponds to its width (L). The upper half of the cosine curve is expressed as "$Y_1 = 0.5H_1 \cos(2\pi x/B_1)$," while the lower half of the cosine curve is expressed as "$Y_2 = 0.5H_2 \cos(4\pi x/B_2)$." Here, t represents the wall thickness of the cell unit, and h denotes its out-of-plane thickness.

Based on Figure 1, a novel cell unit is used to create the two-dimensional multicellular structure shown in Figure 2. The dimensions of the cell unit are as follows: height (H) = 68 mm, width (L) = 80 mm, upper curved edge height (H_1) = 60 mm, lower curved edge height (H_2) = 8 mm, and outer face thickness (h) = 5 mm. The total width of the multicellular structure is 960 mm. The upper and lower rigid plates has a thickness of 10 mm, and the distance between them is 728 mm. The overall structure is composed of 12×12 cells.

To analyse the deformation mechanism of the WA multicellular structure, quasistatic compression simulation analysis of the WA multicellular structure shown in Figure 2 is conducted using the finite element method based on Abaqus software. The nonlinear EXPLICIT dynamic finite element software ABAQUS/EXPLICIT module is used to simulate the dynamic characteristics of in-plane shock. The von Mises yield criterion is assumed to be an ideal elastic-plastic model and is thus followed. Due to the geometric nonlinearity involved in the analysis, the NL Geom is set on in step, and the step size is set automatically. Moreover, to avoid structural penetration after deformation, general contact is defined in the interaction module, and the normal and tangential action behaviours are set as "hard" contact and frictionless, respectively. The model material is aluminium with a density of 2700 kg/m^3, Poisson's ratio of 0.3, modulus of elasticity of 69 GPa, and yield stress of 76 MPa. The multicellular structure in the finite element model is simulated using shell cells (CPS4R), and the upper and lower plates are simulated using solid cells (C3D8R). The

compression direction of the structure is defined as the y-direction, perpendicular to the load direction as the x-direction, and the out-of-plane direction is defined as the z-direction. The upper and lower panels are rigid panels, the upper panel is set with rigid fixed boundary conditions, and the overall deformation of the WA multicellular structure can be visualized as quasistatic compression deformation when the initial velocity of the lower panel is $v_0 = 0.01$ m/s.

According to the Poisson's ratio, a material undergoes elongation or shortening deformation in the load direction and undergoes shortening or elongation deformation in the direction perpendicular to the load. The negative value of the ratio between the strain perpendicular to the load and the strain in the loaded direction is known as Poisson's ratio. The displacement of a multicellular structure in the direction of compression u_y and the displacement perpendicular to the loading direction u_x can thus be calculated, and the equivalent Poisson's ratio of the cellular structure can subsequently be calculated. The specific formula is as follows:

$$\mu_{xy} = -\frac{\varepsilon_x}{\varepsilon_y} = -\frac{u_x L}{u_y W}, \tag{1}$$

where μ_{xy} is the equivalent Poisson's ratio of the multicellular structure; ε_x is the equivalent strain of the multicellular structure in the x direction; ε_y is the equivalent strain of the multicellular structure in the y-direction; u_x is the average displacement of the multicellular structure in the x-direction (mm); u_y is the average displacement of the multicellular structure in the y-direction (mm); L is the length of the quasistatic compression model in the y-direction (mm); and W is the width of the quasistatic compression model in the x-direction (mm). According to equation(1), the equivalent Poisson's ratio of the new structure with respect to the equivalent strain is calculated as shown in Figure 3.

As shown in Figure 3, when $\varepsilon_y = 0.0045$, the novel structure shows an overall positive Poisson's ratio effect in the initial stage of strain; as the strain increases, when $\varepsilon_y = 0.076$, the equivalent Poisson's ratio of the novel structure is approximately 0. When the strain ε_y exceeds 0.076, the novel structure presents a negative Poisson's ratio effect overall. At $\varepsilon_y = 0.059$, the negative Poisson's ratio effect is most obvious, and the equivalent negative Poisson's ratio is −0.38754.

The structure transforms the positive and negative Poisson's ratio effects depending on the deformation compensation between the positive and negative Poisson's ratio cellular elements. The WA cellular unit is periodically extended in the x and y directions to form a multicellular structure, and neighbouring cells can also form cells, as shown in Figure 4.

The cellular structure can be regarded as composed of a W-shaped elastic jumping curved beam and a U-shaped curved beam. The deformation process of a cellular structure compressed in the y-direction is shown in Figure 5. The W-shaped curved beam undergoes elastic buckling deformation from the initial stable state in Figure 5(a) through the transition state in Figure 5(b) and gradually deforms to the second stable state shown in Figure 5(c). When the model is compressed in the y-direction (vertical direction), in the initial stage of this transition process, the W-shaped beam first experiences bending extensile deformation, thus causing the overall structure to exhibit a positive Poisson's ratio effect; as the model is further compressed in the y-direction (vertical direction), at this time, the W-shaped

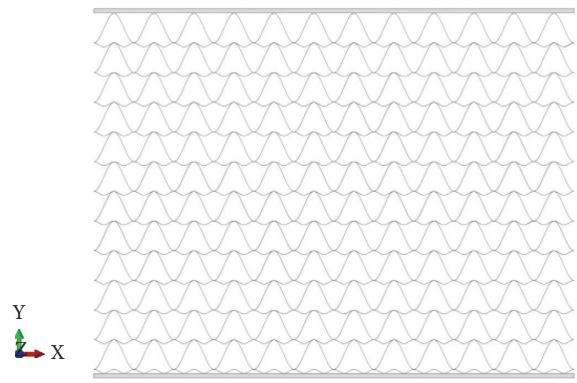

Figure 2: Schematic diagram of the 2D WA multicellular structure.

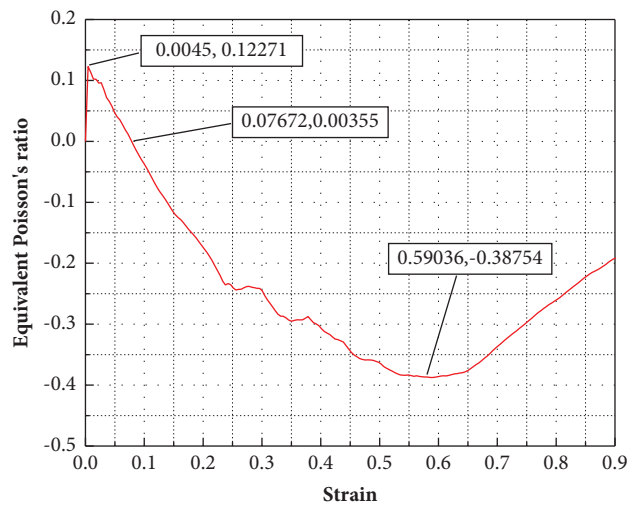

Figure 3: Variation in the equivalent Poisson's ratio of the novel structure with respect to the equivalent strain.

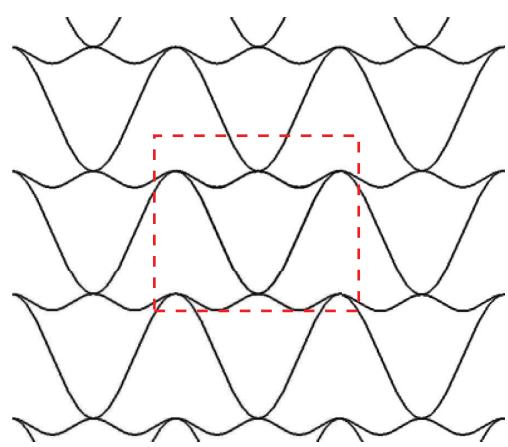

Figure 4: Cellular unit containing a W-shaped curved beam.

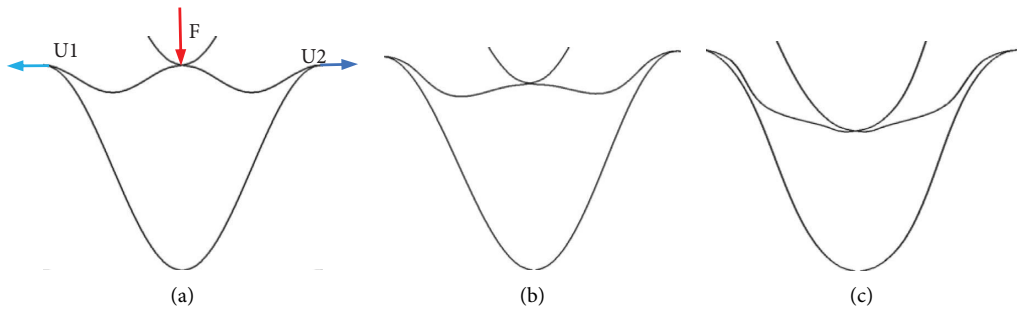

Figure 5: Deformation process of W-shaped curved beam. (a) Initial steady state. (b) Deformation process. (c) Final steady state.

beam gradually transitions to the stable state, resulting in a larger lateral bending retraction deformation and an overall negative Poisson's ratio effect.

2.2. Equivalent Mechanical Parameters of the WA Structure. With reference to the one-dimensional shockwave theory and based on the rigid-perfectly plastic-locking (R-P-P-L) model, Reid et al. proposed a one-dimensional impact model [30–33] assuming that the multicellular material satisfies the R-P-L model and that the maximum impact stress during impact is

$$\sigma_p = \sigma_0 + \frac{\rho_0 v_0^2}{\varepsilon_d}, \tag{2}$$

where ρ_0 is the density of the multicellular material, σ_0 is the plateau stress of the multicellular material, v_0 is the initial impact velocity of the rigid plate, and ε_d is the densification strain of the multicellular structure. The plastic dissipation energy of a multicellular material can be derived from the area enclosed under the stress-strain curve according to the R-P-P-L impact theory as follows:

$$E_p = \frac{1}{2}\left(\sigma_p + \sigma_0\right)\varepsilon_d = \sigma_0\varepsilon_d + \frac{1}{2}\rho_0 v_0^2. \tag{3}$$

The relative density of a multicellular structure is the volume of the multicellular structure V_E and the volume in its envelope space V_H ratio; thus, the relative density of the new WA structure can be calculated according to the following equation:

$$\rho_E = \frac{V_E}{V_H} = \frac{\int_0^L \left(\sqrt{\left(1+\dot{Y}_1^2\right)} + \sqrt{\left(1+\dot{Y}_2^2\right)}\right)\mathrm{dx}}{\mathrm{HL}}, \tag{4}$$

where ρ_E is the equivalent density of honeycomb cellular elements and t is the cellular wall thickness of the multicellular structure. The equivalent density of the novel WA cellular element structure is 0.045, as calculated from equation (4).

Equations (2) and (3) demonstrate that under impact loading, the peak stress increases with increasing impact velocity. The impact velocity is closely related to the dynamic response of multicellular structures, and Hönig and Stronge [34] used the "trapped wave" velocity to define the impact velocity at which the cell element begins to collapse, which is also called the first critical velocity, i.e.,

$$v_w = \int_0^{\varepsilon_w} c(\varepsilon)\mathrm{d}\varepsilon, \tag{5}$$

where

$$c(\varepsilon) = \sqrt{\frac{\sigma'(\varepsilon)}{\rho_0}}, \tag{6}$$

$$\sigma'(\varepsilon) = \frac{d\sigma}{d\varepsilon}. \tag{7}$$

As the impact velocity increases, deformation tends to occur at the impact end of the local deformation and gradually moves towards the fixed end of the propagation of the compression wave in the multicellular material as a class of shock forwards expansion for controlling the collapse of the cell elements. This wave can be called a "stable shock wave." The critical condition for the propagation of a continuous "stabilized shock" wave in multicellular materials can be given by the following equation:

$$v \geq v_s = \sqrt{\frac{2\sigma_0\varepsilon_d}{\rho_0}}, \tag{8}$$

where v_s is also known as the second critical speed.

Equation (8) demonstrates that the critical shock wave velocity depends on the quasistatic platform stress-locked strain and the initial density of the multicellular material. When the impact velocity $v0$ is smaller than the first critical velocity for the low-velocity impact, the multicellular structure can be considered to experience quasistatic deformation. The impact velocity is lower than the second critical velocity and greater than the first critical velocity for medium-velocity impact. At this time, the cellular element deformation mode for the transition stage deformation occurs when the impact velocity is greater than the second critical velocity for the high-velocity impact. The first critical velocity of the multicellular structure is approximately 12.4 m/s, and the second critical velocity is approximately 93 m/s; these values are calculated by equations (5)–(8). To ensure that the deformation mode covers the three deformation intervals of low, medium, and high speeds, four impact velocities, namely, 10 m/s, 25 m/s, 50 m/s, and 100 m/s, are selected for the simulation and analysis of the in-plane impact on the new WA multicellular structure.

Figure 6 shows the calculated variation in the equivalent Poisson's ratio of the novel WA multicellular structure for different impact velocities.

As shown in Figure 6, the initial positive Poisson's ratio effect of the structure is not obvious at all stages of compression under different impact velocity conditions because the velocity of the in-plane impact load is relatively high compared to that of the quasistatic action, and the negative Poisson's ratio deformation of the W-shaped curved beam occurs very quickly under inertia, so the structure exhibits an obvious negative Poisson's ratio effect. Under different speed conditions, the absolute value of the structural equivalent Poisson's ratio increases and then decreases as the equivalent strain increases, and the maximum value of the absolute value of the equivalent Poisson's ratio decreases as the impact velocity increases. When the impact velocity is 10 m/s, the negative Poisson's ratio effect on the multicellular structure is the most significant; when the impact velocity is 100 m/s, the multicellular structure undergoes layer-by-layer compression collapse damage, and the overall negative Poisson's ratio effect almost disappears.

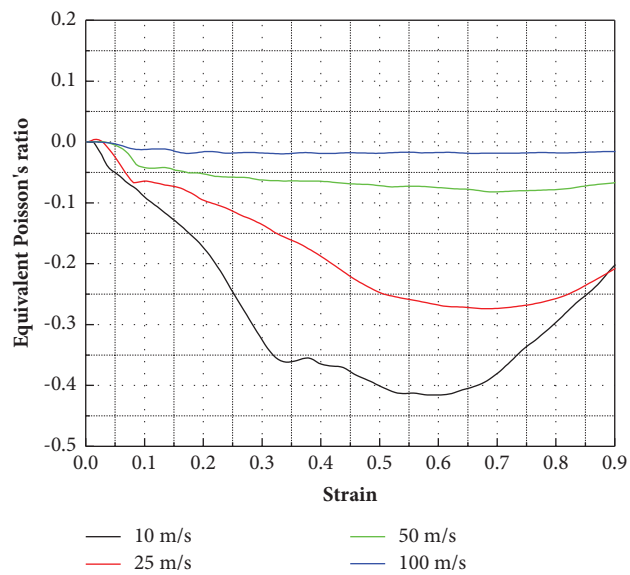

Figure 6: Variation in the equivalent Poisson's ratio of the novel WA multicellular structure at different impact velocities.

2.3. Deformation Patterns of the WA Multicellular Structure. The deformation pattern of the structure can reflect its energy absorption mechanism; for this reason, in this paper, the deformation patterns of the novel WA multicellular structure under different impact velocities are analysed. Figure 7 shows the deformation patterns of the new WA multicellular structure under four different impact velocities.

As shown in Figure 7, the deformation modes of the structure can be roughly categorized into three types as follows: "overall" deformation modes, "transition" deformation modes, and "local collapse" deformation modes.

When the impact velocity is 10 m/s, the WA multicellular structure exhibits the "whole" deformation mode. First, under the action of an in-plane impact load, the curved beams in the middle and lower layers of the cellular structure undergo bending deformation. At this time, the middle part of the multicellular structure is concave overall, exhibiting an obvious negative Poisson's ratio effect. Under the continuous action of an in-plane impact load, the curved beams are transformed from bending to flexure deformation, and at this time, the multicellular structure gradually densifies under the compression of the rigid plate.

When the impact velocity is 25 m/s or 50 m/s, the WA multicellular structure is in the "transition" deformation mode. The multicellular structure forms a local deformation zone at the impact end, and the overall structure also deforms; as the impact velocity increases, the "local" deformation characteristics of the "impact end" gradually increase, while the "overall" deformation characteristics gradually weaken. In this deformation mode, the multicellular structure still exhibits a negative Poisson's ratio under small strain.

When the impact velocity is 100 m/s, the WA multicellular structure experiences "local collapse." In this mode, the impact end first forms a local deformation zone, and under the action of inertia, the impact end exhibits the deformation mode of layer-by-layer collapse, which gradually propagates to the fixed end. In this deformation mode, the multicellular structure no longer exhibits an obvious negative Poisson's ratio effect.

3. WA Multicellular Pedestal Performance Analysis

The pedestal is the connecting support structure between the equipment and the hull. It should have a large bearing capacity and resistance to external impact. The established WA multicellular model based on the novel WA multicellular structure for establishing the equipment impact resistance pedestal is depicted in Figure 8. The pedestal model consists of the upper and lower panels and the new WA multicellular structure. The size of the upper panel of the pedestal is $400 \times 500 \times 3$ mm, and the size of the lower panel is $640 \times 500 \times 3$ mm. During the modelling process, a centralized mass unit is used to simulate the equipment on the pedestal, with the mass of the equipment being 0.2 t and the centre of gravity being 200 mm above the upper panel. A spring unit is used to simulate the vibration isolator.

3.1. Pedestal Bearing Capacity Analysis. The strength and stiffness of equipment pedestals are related to the stability and safety of the equipment. When installing the equipment, the equipment pedestal needs to have a large bearing capacity, and the deformation of the pedestal needs to be controlled. The cellular structure of WA is similar to the double-arrow cellular structure, and several researchers have used the double-arrow cellular structure to establish the equipment pedestal. Therefore, in this paper, models of both a double-arrow multicellular base and a WA multicellular base with the same cell size are established based on the finite element analysis software Abaqus. The maximum deformation and stress state of the base under an equipment gravity load are calculated. Figures 9 and 10 show the

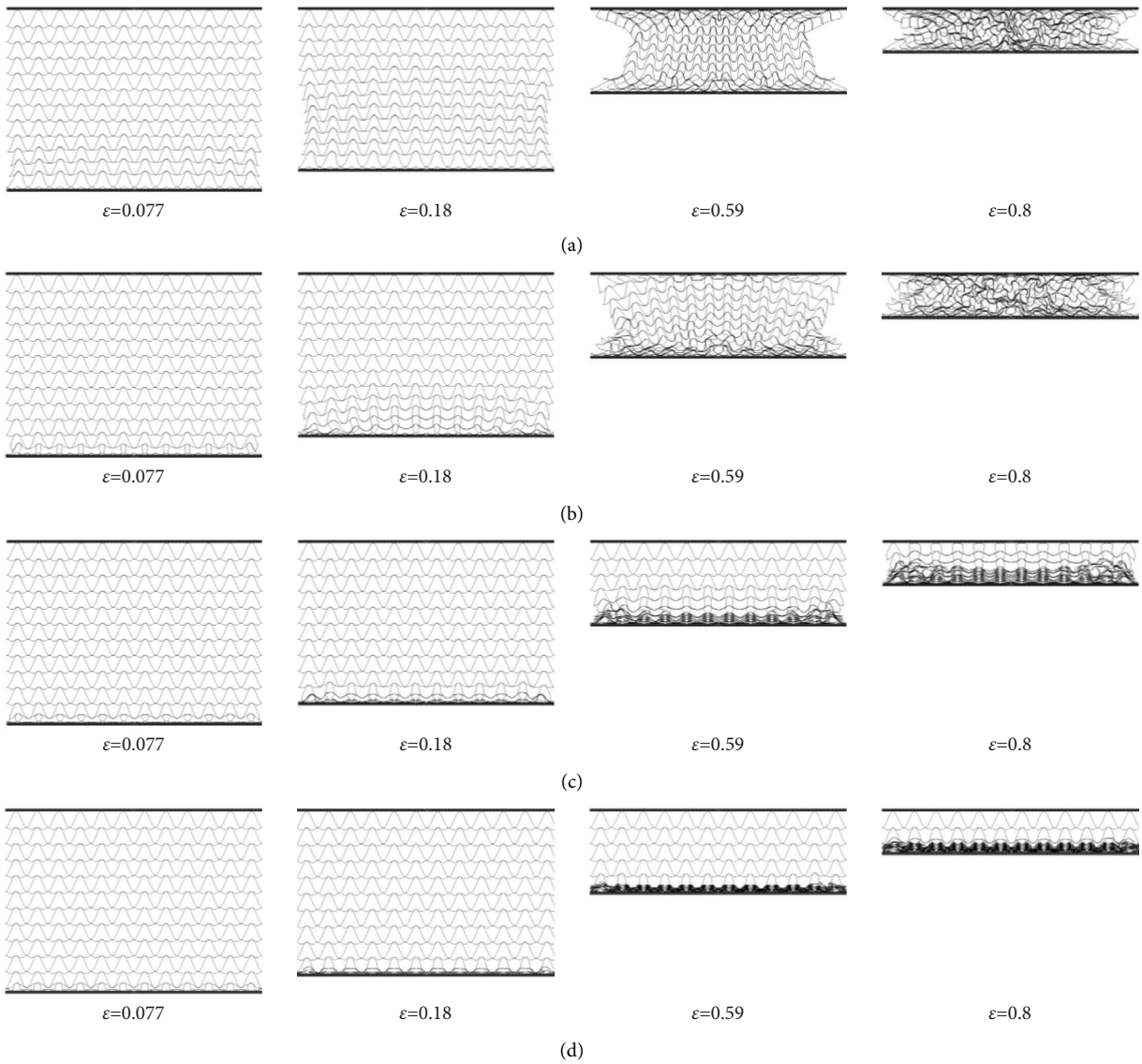

Figure 7: Deformation pattern of the novel WA multicellular structure. (a) Impact velocity of 10 m/s. (b) Impact velocity of 25 m/s. (c) Impact velocity of 50 m/s. (d) Impact velocity 100 m/s.

displacement cloud map and stress cloud map of the base structure under the influence of the gravitational load. Table 1 shows the maximum displacement and von Mises stress values of the two bases under static loading.

Figures 7 and 8 and Table 1 demonstrate that the WA multicellular pedestal exhibits a maximum displacement of 0.0158 mm under the gravitational load of the equipment. This displacement occurs in the upper layer of the pedestal structure. Furthermore, the displacement and deformation of the WA multicellular pedestal are smaller than those of the double-arrow multicellular pedestal. This indicates that the WA multicellular pedestal has a greater bearing capacity than the double-arrow multicellular pedestal. The maximum stress experienced by the WA multicellular pedestal is 4.105 MPa, which occurs at the connection point between cellular elements within its structure. This value complies with the permissible material stress (235 MPa). In addition, its maximum von Mises stress and stress distribution are more uniform and less pronounced in magnitude than those of the double-arrow multicellular pedestal.

3.2. Analysis and Optimization of Pedestal Impact Performance. A pedestal with excellent impact protection can provide a stable working environment for equipment. In this paper, the impact resistance of the novel pedestal is verified using an acceleration impact load according to the German military specification BV043/85.

Shock loading involves converting a shock spectrum based on a frequency domain description into a time domain acceleration and loading the equipment pedestal with the converted acceleration time course profile as a shock load. Figure 11 shows the triple-fold shock spectrum as specified in the German military specification BV043/85.

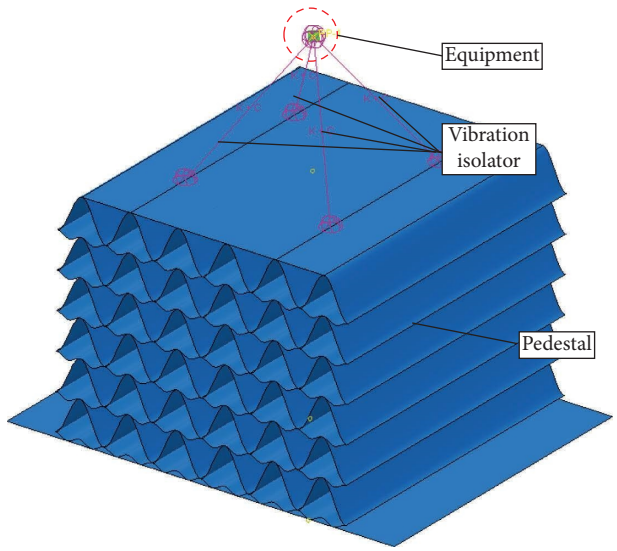

Figure 8: WA multicellular pedestal.

Table 1: Maximum pedestal displacement and von Mises stresses.

	Double-arrow multicellular pedestal	WA multicellular pedestal
Maximum Mises stress (MPa)	4.240	4.105
Maximum displacement (mm)	$1.796e-2$	$1.585e-2$

As shown in Figure 11, the impact spectrum consists of an equal displacement section, equal velocity section, and equal acceleration section. When the mass of the equipment is less than $5\,t$, the value of the equal acceleration spectrum $A_0 = 320\,g$, the value of the equal velocity spectrum $V_0 = 7$ m/s, and the value of the equal displacement spectrum $D_0 = 0.043$ m in the vertical impact environment. According to the specification of BV043/85, the positive and negative triangular waves are calculated as shown in Figure 12. Its relevant parameters are $a_1 = 192\,g$, $a_2 = -102\,g$, $t_1 = 0.0022$ s, $t_2 = 0.0056$ s, $t_3 = 0.0119$ s, and $t_4 = 0.0161$ s.

The impact resistance of the pedestal structure is analysed using the large mass method. In this analysis, a mass of $3.4 \times 10^6\,t$ is assigned to the large mass point. The large mass point serves as the active point, and the concentrated force load is considered equivalent to an acceleration impact load. The MPC connection method is used to connect the following panel to the slave region. The acceleration impact load shown in Figure 12 is applied to the large mass point, and the average acceleration response of typical measurement points on the upper panel of the pedestal structure is then calculated to evaluate its impact resistance performance. The impact resistance is evaluated accordingly. Figure 13 illustrates how the impact load is loaded and where the response evaluation points are located, while Figure 14 displays the calculated average acceleration response at the measurement points.

Figure 14 illustrates that the maximum value of the acceleration response of the upper panel is 2865.02 m/s^2. The different parameters of the pedestal structure directly influence the impact resistance of the structure. To identify the optimal combination of pedestal structure parameters for impact resistance, optimization analysis is conducted for the width of the cell element, the length of the upper curved edge of the cell element, the length of the lower curved edge of the cell element, the thickness of the upper panel, the thickness of the lower panel, and the cell wall element thickness. The minimum mean value of the acceleration response at the structural response evaluation point shown in Figure 13 is selected as the optimization objective. As a constraint, the pedestal stress is set to be less than the allowable stress of the structure, and the multiparameter optimization model shown in the following equation is established.

$$\begin{cases} \text{Find} & X = [H_1, H_2, B_1, T_1, T_2, T_3], \\ \text{Min} & F(x) = \max(A), \\ S.T. & \sigma < [\sigma], \end{cases} \tag{9}$$

where A is the mean value of the acceleration response and $[\sigma]$ is the allowable stress of the material, which is set as 235 MPa.

The parameters of the pedestal structure are optimized using a multi-island genetic algorithm. The optimization ranges for the variables of the pedestal structure during this process are presented in Table 2, and the acceleration response optimization process is depicted in Figure 15. The optimal solution is obtained after 191 iterations. The initial parameters corresponding to this optimal solution are presented in Table 3.

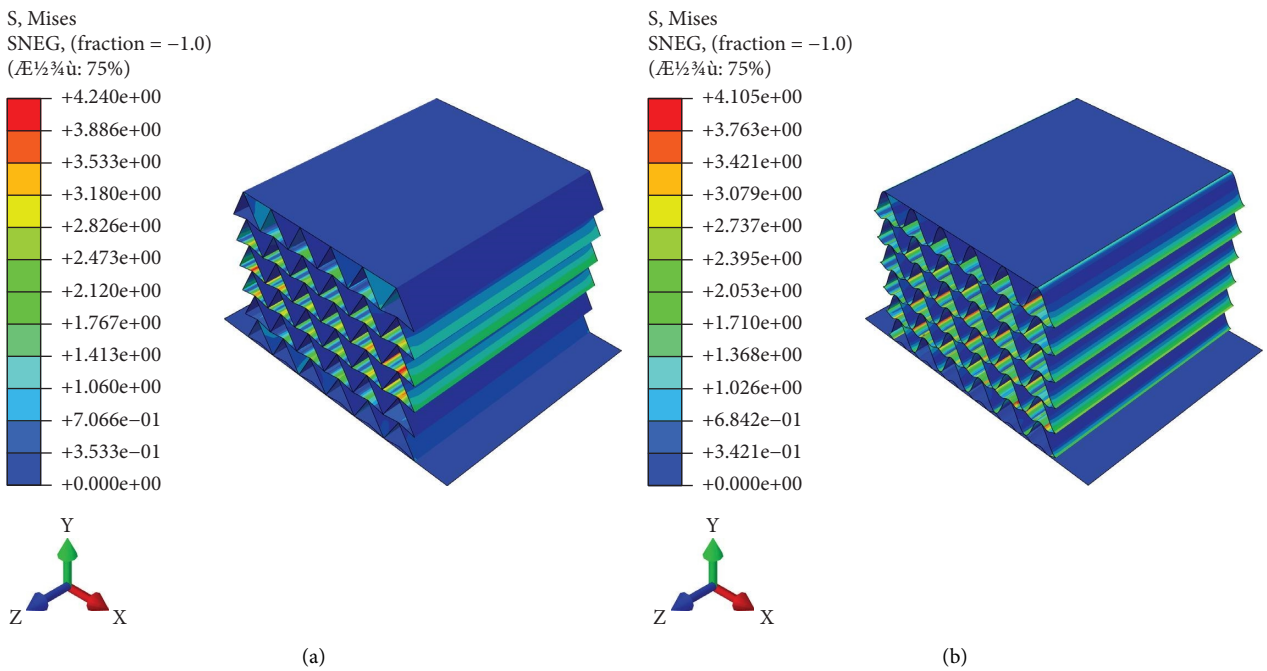

Figure 9: Pedestal stress cloud. (a) Double-arrow multicellular pedestal stress cloud. (b) WA multicellular pedestal stress cloud.

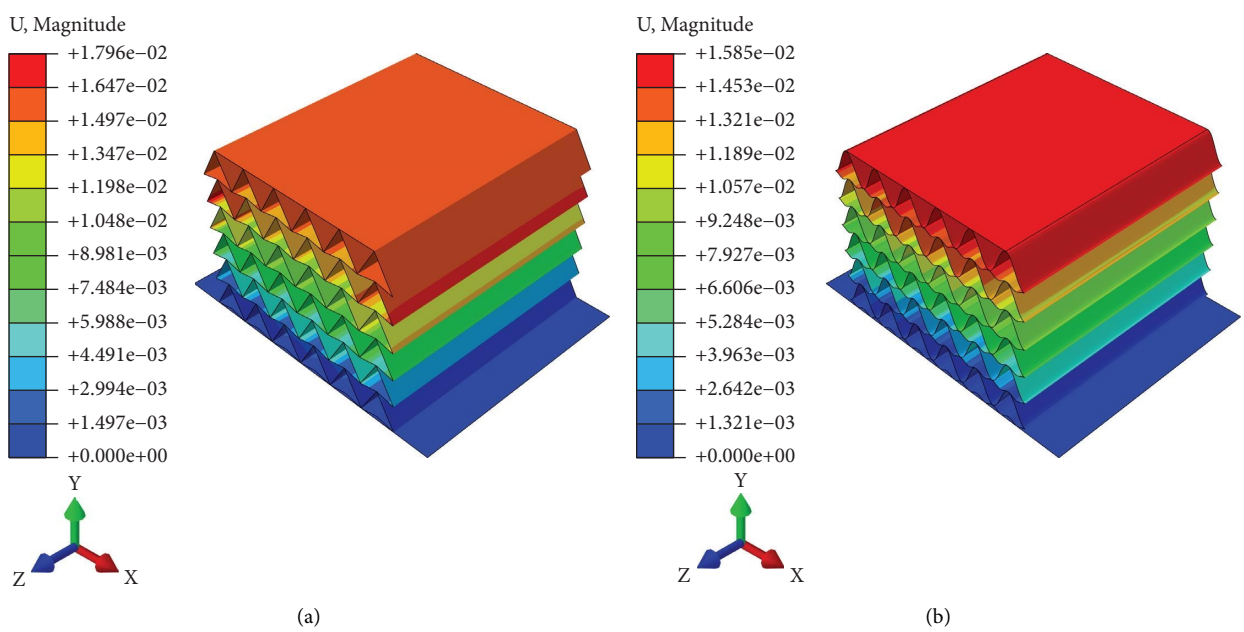

Figure 10: Cloud diagram of pedestal displacement. (a) Double-arrow multicellular pedestal displacement cloud. (b) WA multicellular pedestal displacement cloud.

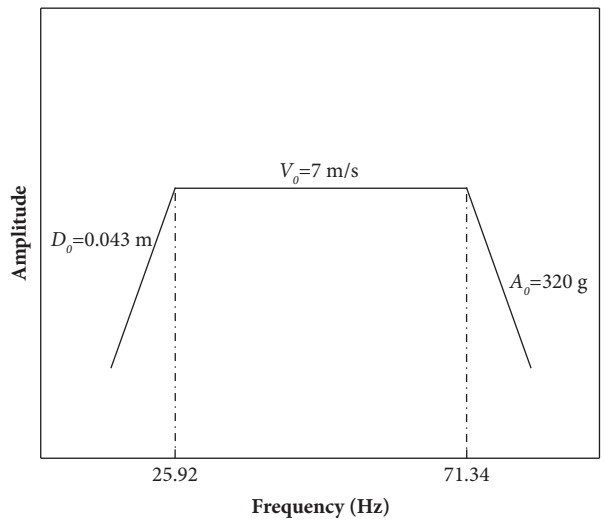

Figure 11: Schematic diagram of a trifold spectrum.

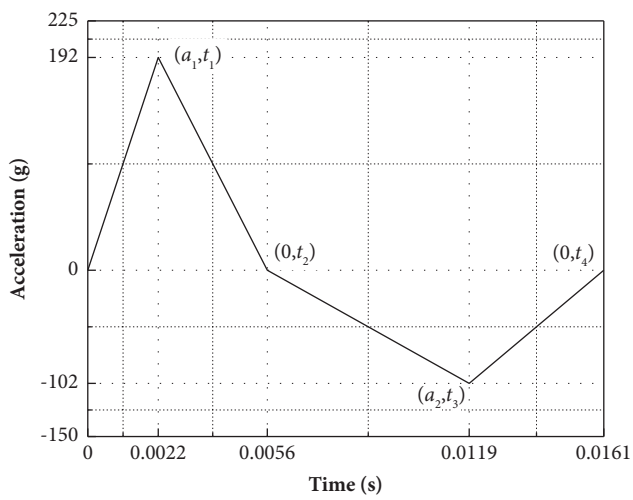

Figure 12: Impact load-time course curve.

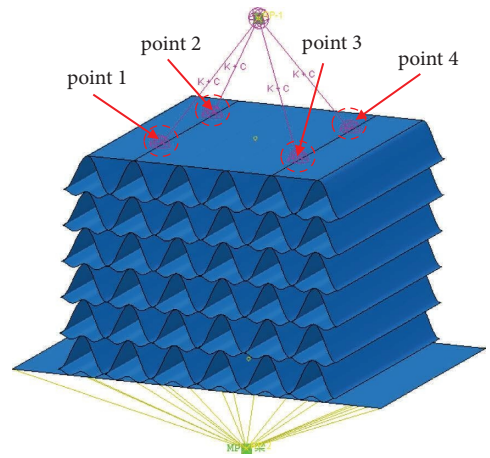

Figure 13: Impact load loading mode and response evaluation point.

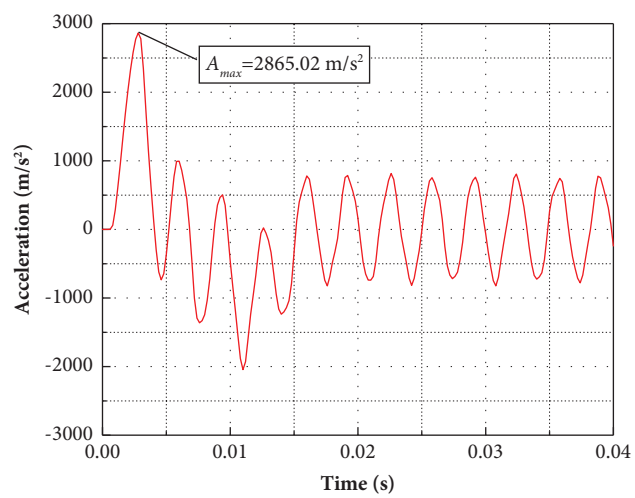

Figure 14: Mean value of acceleration response of measurement points.

The data in Table 3 illustrate that the maximum acceleration response values of the panel on the pedestal before and after optimization are 2865.02 m/s^2 and 1851.04 m/s^2, respectively. The peak acceleration of the panel on the pedestal is reduced by 35.39% through optimization.

4. Impact Experiments on a Novel Multicellular Pedestal Model

To evaluate the impact resistance of the WA multicellular pedestal designed in this paper, experiments were conducted using the QCXP-200A pneumatic horizontal shock test system to load the WA multicellular pedestal model with a horizontal impact load. The maximum shock response acceleration that can be generated by the shock test system is 10,000 g, and the frequency range of the response spectra calculation is from 10 Hz to 8 kHz. The shock test platform and the pedestal model are shown in Figure 16. The base model is made of Q235 steel, and Q235 square steel mass blocks are used to simulate the equipment. Four equipment mass blocks, each weighing 3.3 kg, were used. The overall dimensions of the base were 300 × 180 × 246 mm, and the cell wall thickness was 2 mm. The top panel measures 240 × 180 × 3 mm, and the bottom panel measures 360 × 230 × 4 mm. The bottom end of the base is fixed to the impact platform, and the upper end is connected to the square mass block through bolt connections.

During the experiment, acceleration response measurement points are arranged in the centre of the upper panel, the centre of the lower panel, and the impact test platform surface of the pedestal to measure the response of the structure under the impact load, and the sampling frequency is set to 10 kHz. The sensor placement is shown in Figure 17.

The response spectrum of the impact load obtained from the accelerometer placed on the tabletop is shown in Figure 18. The response spectrum is analysed in the frequency range of 20–5120 Hz.

The time-course response of the acceleration of the structure under impact loading, as measured by the accelerometers placed at the centre of the upper panel, the centre of the lower panel, and the impact test platform, is shown in Figure 19.

Table 2: Initial values of the design variables and optimization range.

Design variable	Variable name	Initial value	Optimization range
H_1 (mm)	Upper curved edge height	60	(50, 100)
H_2 (mm)	Lower curved edge height	8	(6, 20)
B_1 (mm)	Cell width	80	(50, 100)
T_1 (mm)	Upper panel thickness	3	(2, 5)
T_2 (mm)	Cell wall thickness	3	(2, 5)
T_3 (mm)	Lower panel thickness	3	(2, 5)

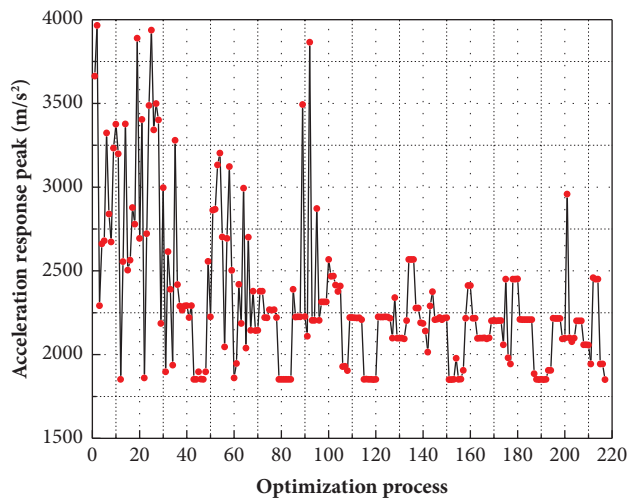

Figure 15: Acceleration response optimization history.

Table 3: Values of the design variables before and after optimization.

	H_1 (mm)	H_2 (mm)	B_1 (mm)	T_1 (mm)	T_2 (mm)	T_3 (mm)	Acceleration response $(m/s)^2$
Preoptimization	60	8	80	3	3	3	2865.02
Postoptimization	88	16	68	4	5	2	1851.04

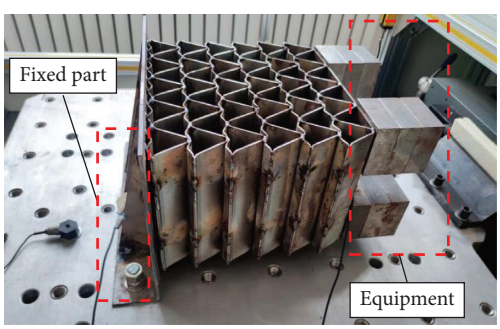

Figure 16: Impact test platform and pedestal model.

Figure 19 illustrates that the shock response is divided into an obvious initial response stage and a residual response stage. In the initial response phase, the acceleration initial response peaks appear in the following temporal order: the response table, lower panel, and upper panel. The acceleration initial response peaks are the impact test platform, lower panel, and upper panel in the descending order, indicating that the WA multicellular pedestal greatly reduces the input shock loads.

Figure 20 shows the pneumatic buffers on both sides of the impact test platform. In the residual response phase after impact, the peak accelerations from largest to smallest are as follows: upper panel, lower panel, and impact test platform. This is because the pneumatic buffers on both sides of the platform restrict the vibration of the impact platform, causing its response amplitude to rapidly attenuate. The WA multicellular pedestal is distant from the impact end and is in a free state. Free vibration occurs after impact, and the response of the upper panel is slower than that of the table surface and the lower panel attenuation.

For the WA structure designed in this paper, the curved structure can overcome the shortcomings of the straight edge structure to a certain extent, but its special curve configuration increases the difficulty of numerical analysis and brings difficulties to model development. It is difficult to weld steel plates between cells, and the precision is difficult to control because of the deformation of the weld. Although metal 3D printing technology is convenient to manufacture, the cost is high, which significantly limits the wide application of negative Poisson's ratio structures; therefore, determining how to achieve mass production at a lower cost is still a key problem to be studied.

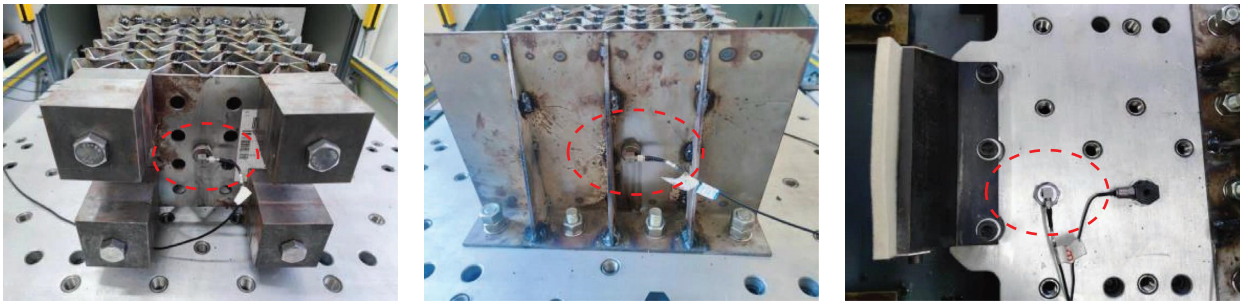

(a) (b) (c)

Figure 17: Schematic diagram of measurement point arrangement. (a) Upper panel measurement points. (b) Lower panel measurement points. (c) Impact test platform measurement points.

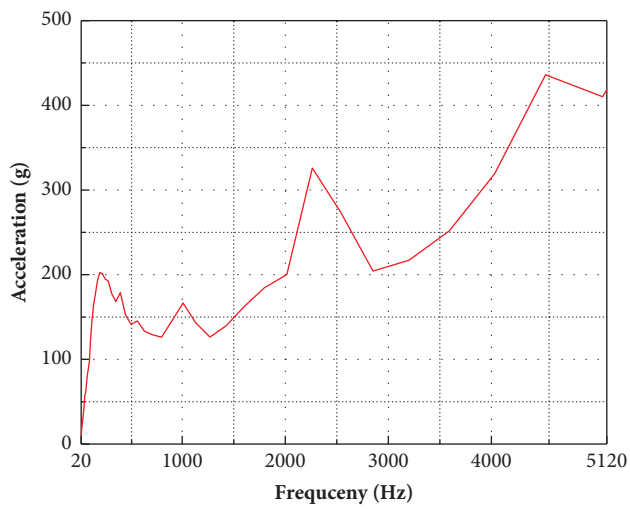

Figure 18: Shock response spectrum.

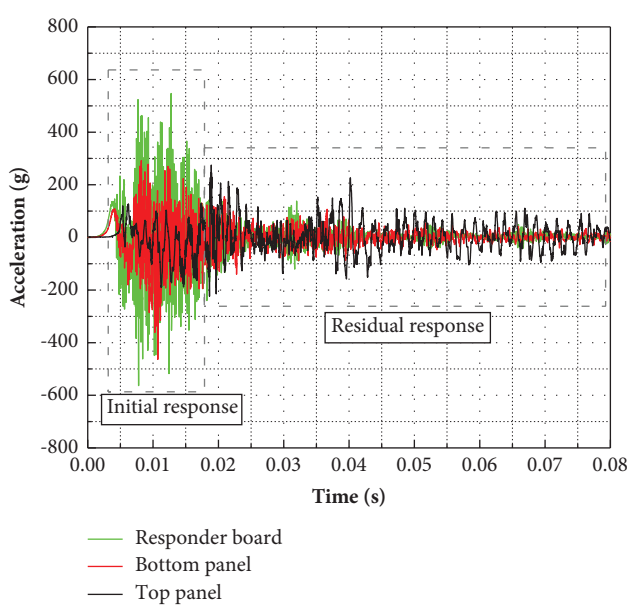

Figure 19: Experimental acceleration response plots.

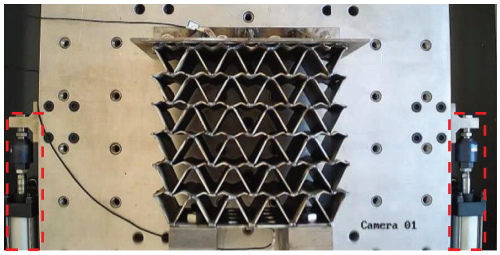

Figure 20: Pneumatic buffers on both sides of the impact test platform.

5. Summary

Considering the ship equipment pedestal load carrying capacity and impact resistance demands, a novel positive and negative Poisson's ratio structure is proposed in this paper. The novel WA multicellular structure forms a W-shaped curved beam at the cell unit connection so that it has a positive Poisson's ratio effect in the initial stage of elastic deformation, exhibiting a better static load carrying capacity. As the y-direction continues to compress, the overall structure exhibits a negative Poisson's ratio effect, which results in a better antiimpact performance. Using the novel WA multicellular structure to establish the equipment impact pedestal and the multiparameter optimization of the pedestal structure parameters through a multi-island genetic algorithm, the peak acceleration decreases by 35.39% through the optimization of the pedestal structure. An impact experimental study is conducted on the pedestal structure designed in this paper, and the experimental results show that the proposed impact-resistant pedestal structure can effectively absorb the impact load. This research offers new insights into designing impact-resistant ship structure pedestals.

Data Availability

The data that support the findings of this study are available upon request from the corresponding author.

Conflicts of Interest

The authors declare that they have no conflicts of interest.

Acknowledgments

This work was supported by the National Natural Science Foundation of China (grant nos. U20A20327 and 52271265).

References

[1] Z. Yan, Y. Liu, J. Yan et al., "Anti-blast performance of 3D-printed sandwich panels with auxetic hexagonal and regular hexagonal honeycomb cores," *Engineering Structures*, vol. 272, Article ID 114996, 2022.

[2] Y. Ma, D. Wang, H. Cheng, and Y. Shi, "Bayesian theory-based seismic failure modes identification of reinforced concrete columns," *Journal of Earthquake Engineering*, vol. 26, no. 13, pp. 6703–6723, 2022.

[3] Y. Ma, Z. Wu, Z. Liu, M. Zhang, and M. Aibaidula, "Seismic fragility analysis of aqueduct structural systems based on G-PCM method," *Sustainability*, vol. 14, 2022.

[4] Z. Wang, S. Yao, Z. Lu, D. Hui, and L. Feo, "Matching effect of honeycomb-filled thin-walled square tube—experiment and simulation," *Composite Structures*, vol. 157, pp. 494–505, 2016.

[5] C. Xia, Z. Zhang, C. Liu, H. Zhang, and S. Tian, "Study on numerical model and dynamic response of ring net in flexible rockfall barriers," *Sustainability*, vol. 14, no. 8, p. 4406, 2022.

[6] J. Yang, S. Duan, Q. Li, and C. Liu, "A review of flexible protection in rockfall protection," *Natural Hazards*, vol. 99, no. 1, pp. 71–89, 2019.

[7] R. P. Bohara, S. Linforth, A. Ghazlan, T. Nguyen, A. Remennikov, and T. Ngo, "Performance of an auxetic honeycomb-core sandwich panel under close-in and far-field detonations of high explosive," *Composite Structures*, vol. 280, Article ID 114907, 2022.

[8] M. F. Guo, H. Yang, and L. Ma, "Design and characterization of 3D AuxHex lattice structures," *International Journal of Mechanical Sciences*, vol. 181, Article ID 105700, 2020.

[9] J. A. Harris and G. J. McShane, "Impact response of metallic stacked origami cellular materials," *International Journal of Impact Engineering*, vol. 147, Article ID 103730, 2021.

[10] R. Jafari Nedoushan, Y. An, W. R. Yu, and M. J. Abghary, "Novel triangular auxetic honeycombs with enhanced stiffness," *Composite Structures*, vol. 277, Article ID 114605, 2021.

[11] X. Y. Zhang, X. Ren, Y. Zhang, and Y. M. Xie, "A novel auxetic metamaterial with enhanced mechanical properties and tunable auxeticity," *Thin-Walled Structures*, vol. 174, Article ID 109162, 2022.

[12] W. Zhang, S. Zhao, F. Scarpa, J. Wang, and R. Sun, "In-plane mechanical behavior of novel auxetic hybrid metamaterials," *Thin-Walled Structures*, vol. 159, Article ID 107191, 2021.

[13] L. Wei, X. Zhao, Q. Yu, and G. Zhu, "A novel star auxetic honeycomb with enhanced in-plane crushing strength," *Thin-Walled Structures*, vol. 149, Article ID 106623, 2020.

[14] Q. Gao, C. Ge, W. Zhuang, L. Wang, and Z. Ma, "Crashworthiness analysis of double-arrowed auxetic structure under axial impact loading," *Materials and Design*, vol. 161, pp. 22–34, 2019.

[15] M. F. Guo, H. Yang, and L. Ma, "3D lightweight double arrow-head plate-lattice auxetic structures with enhanced stiffness and energy absorption performance," *Composite Structures*, vol. 290, Article ID 115484, 2022.

[16] C. Qi, L. Z. Pei, A. Remennikov, S. Yang, and F. Jiang, "Numerical and theoretical analysis of crushing strength of 3D re-entrant honeycomb," *Thin-Walled Structures*, vol. 182, Article ID 110140, 2023.

[17] H. Jiang, Y. Ren, Q. Jin, G. Zhu, Y. Hu, and F. Cheng, "Crashworthiness of novel concentric auxetic reentrant honeycomb with negative Poisson's ratio biologically inspired by coconut palm," *Thin-Walled Structures*, vol. 154, Article ID 106911, 2020.

[18] N. Novak, M. Vesenjak, S. Tanaka, K. Hokamoto, and Z. Ren, "Compressive behaviour of chiral auxetic cellular structures at different strain rates," *International Journal of Impact Engineering*, vol. 141, Article ID 103566, 2020.

[19] S. Tabacu, R. F. Negrea, and D. Negrea, "Experimental, numerical and analytical investigation of 2D tetra-anti-chiral structure under compressive loads," *Thin-Walled Structures*, vol. 155, Article ID 106929, 2020.

[20] L. J. Gibson, M. F. Ashby, G. S. Schajer, and C. I. Robertson, "The mechanics of two-dimensional cellular materials," *Proceedings of the Royal Society of London. A Mathematical and Physical Sciences*, vol. 382, no. 1782, pp. 25–42, 1982.

[21] J. N. Grima, R. Gatt, A. Alderson, and K. E. Evans, "On the potential of connected stars as auxetic systems," *Molecular Simulation*, vol. 31, no. 13, pp. 925–935, 2005.

[22] H. Wang, Z. Lu, Z. Yang, and X. Li, "A novel re-entrant auxetic honeycomb with enhanced in-plane impact resistance," *Composite Structures*, vol. 208, pp. 758–770, 2019.

[23] X. T. Wang, B. Wang, X. W. Li, and L. Ma, "Mechanical properties of 3D re-entrant auxetic cellular structures," *International Journal of Mechanical Sciences*, vol. 131, pp. 396–407, 2017.

[24] M. Fu, F. Liu, and L. Hu, "A novel category of 3D chiral material with negative Poisson's ratio," *Composites Science and Technology*, vol. 160, pp. 111–118, 2018.

[25] A. Alomarah, D. Ruan, S. Masood, I. Sbarski, and B. Faisal, "An investigation of in-plane tensile properties of re-entrant chiral auxetic structure," *The International Journal of Advanced Manufacturing Technology*, vol. 96, no. 5-8, pp. 2013–2029, 2018.

[26] Y. Wang, W. Zhao, G. Zhou, Q. Gao, and C. Wang, "Optimization of an auxetic jounce bumper based on Gaussian process metamodel and series hybrid GA-SQP algorithm," *Structural and Multidisciplinary Optimization*, vol. 57, no. 6, pp. 2515–2525, 2018.

[27] G. Imbalzano, S. Linforth, T. D. Ngo, P. V. S. Lee, and P. Tran, "Blast resistance of auxetic and honeycomb sandwich panels: comparisons and parametric designs," *Composite Structures*, vol. 183, pp. 242–261, 2018.

[28] Z. Song, H. Liang, H. Ding, and M. Ma, "Structure design and mechanical properties of a novel anti-collision system with negative Poisson's ratio core," *International Journal of Mechanical Sciences*, vol. 239, Article ID 107864, 2023.

[29] W. Liu, N. Wang, T. Luo, and Z. Lin, "In-plane dynamic crushing of re-entrant auxetic cellular structure," *Materials and Design*, vol. 100, pp. 84–91, 2016.

[30] S. R. Reid and C. Peng, "Dynamic uniaxial crushing of wood," *International Journal of Impact Engineering*, vol. 19, no. 5-6, pp. 531–570, 1997.

[31] J. J. Harrigan, S. R. Reid, and A. Seyed Yaghoubi, "The correct analysis of shocks in a cellular material," *International Journal of Impact Engineering*, vol. 37, no. 8, pp. 918–927, 2010.

[32] P. J. Tan, J. J. Harrigan, and S. R. Reid, "Inertia effects in uniaxial dynamic compression of a closed cell aluminium alloy foam," *Materials Science and Technology*, vol. 18, no. 5, pp. 480–488, 2002.

[33] P. J. Tan, S. R. Reid, J. J. Harrigan, Z. Zou, and S. Li, "Dynamic compressive strength properties of aluminium foams. Part II—'shock' theory and comparison with experimental data and numerical models," *Journal of the Mechanics and Physics of Solids*, vol. 53, no. 10, pp. 2206–2230, 2005.

[34] A. Hönig and W. J. Stronge, "In-plane dynamic crushing of honeycomb. Part I: crush band initiation and wave trapping," *International Journal of Mechanical Sciences*, vol. 44, no. 8, pp. 1665–1696, 2002.